Control Engineering Practice 156 (2025) 106234

Contents lists available at ScienceDirect

Control Engineering Practice

journal homepage: www.elsevier.com/locate/conengprac

A force controller for valve-manipulated hydraulic actuators

Yuki Yamamoto [a,b,*], Ryo Kikuuwe [a]

[a] Machinery Dynamics Laboratory, Hiroshima University, 1-4-1 Kagamiyama, Higashi-Hiroshima, 739-8527, Hiroshima, Japan
[b] Japan Society for the Promotion of Science, Japan

ARTICLE INFO

Keywords:
Force control
Hydraulic actuator
Admittance control
Deadtime
Time delay
Energy-based stabilization

ABSTRACT

This paper proposes a force controller for hydraulic actuators of the valve-manipulated type. The structure of the proposed controller is similar to that of the admittance controllers used for robotic systems, incorporating a virtual mass–damper system that transforms the measured force to the reference velocity. In the proposed controller, the reference velocity is transformed into the valve opening commands through a quasi-static hydraulic actuator model. This paper also proposes an energy-based stabilizer that imposes limits on the reference velocity to prevent the instability induced by the deadtime, which commonly exists in hydraulic systems. The proposed controller, combined with the stabilizer, is validated with a laboratory setup composed of a linear hydraulic actuator that makes contact with a stiff external environment.

1. Introduction

Hydraulic actuators are widely used in various types of machinery, including construction machinery, press machines, and legged robots (Boaventura, Buchli, Semini, & Caldwell, 2015; Hyon, Suewaka, Torii, & Oku, 2017; Yu et al., 2019). Hydraulic actuators are classified into some types by their operating schemes; some are operated by manipulating pump flowrate (Ahn, Chau, & Truong, 2007; Ahn & Dinh, 2009; Liem, Truong, Park, & Ahn, 2016; Truong & Ahn, 2009), some by manipulating valve opening ratios (Ruderman, Fridman, & Pasolli, 2019) and some others by both (Yu et al., 2020). This paper focuses on the valve-manipulated type, which is commonly used in commercially available excavators (Yamamoto et al., 2024, 2021) and their attachments, such as grapples and nibblers.

Some applications of hydraulic actuators involve contact with environments or external objects, and thus appropriate controllers to regulate the contact forces are needed. For controlling the contact force, admittance control is one of the well-known approaches especially for industrial robots driven by electromagnetic actuators (Ferraguti et al., 2019; Haninger, Radke, Vick, & Kruger, 2022; Kikuuwe, 2019; Liu, He, Chen, & Cao, 2022). An admittance controller receives the inputs of a measured external force and a target force, and converts them into a reference position signal. The reference position is used as the input to an internal positional controller, a part of the admittance controller, which forces the actuator to track the reference position. Such control schemes have also been used with hydraulic actuators (Chae, Rabiee, Dursun, & Kim, 2017; Chen, Chen, & Yao, 2018; Chen et al., 2017; Heinrichs, Sepehri, & Thornton-Trump, 1997; Sivaselvan, Reinhorn, Shao, & Weinreber, 2008; Zhong, Li, Gao, & Dong, 2021). The conversion from the measured forces to the position could be performed by a virtual mass–damper–spring system (Heinrichs et al., 1997), a virtual spring-damper system (Zhong et al., 2021), a virtual spring (Chae et al., 2017; Sivaselvan et al., 2008), or a kind of integral controller (Chen et al., 2018, 2017). A good side of admittance control schemes is that the response characteristics can be easily adjusted by tuning stiffness, viscosity, and mass parameters, which are physically understandable. It however requires careful tuning of the internal controller because improper gain setting may lead to severe performance degradation or even instability.

As another approach, there are force controllers based on the models of the hydraulic actuators. In such controllers, the accuracy of the models directly affects control performance. Therefore, these force controllers are combined with techniques to compensate for the modeling errors, such as a neural-network-based disturbance observer (Yang & Yao, 2022), adaptive control (Alleyne & Liu, 2000; Cheng et al., 2020; Yao, Jiao, & Yao, 2014; Yao, Jiao, Yao, Shang, & Dong, 2012; Zhu & Piedboeuf, 2004), a gain scheduling (Dakova, Sawodny, & Böhm, 2024), and model-predictive control (Essa, Aboelela, Moustafa Hassan, & Abdrabbo, 2018, 2019; Yuan, Na, & Kim, 2018). In addition, there are force controllers based on robust-control design, such as the quantitative feedback theory (Niksefat & Sepehri, 2001) and sliding-mode control (Jerouane, Sepehri, & Lamnabhi-Lagarrigue, 2004). In some force controllers (He, 2009; Kim et al., 2021), the relation between the actuator force and the valve command is estimated using neural networks. These model-based force controllers have been successful

* Corresponding author at: Machinery Dynamics Laboratory, Hiroshima University, 1-4-1 Kagamiyama, Higashi-Hiroshima, 739-8527, Hiroshima, Japan.
E-mail address: y.yamamoto@mdl.hiroshima-u.ac.jp (Y. Yamamoto).

https://doi.org/10.1016/j.conengprac.2024.106234
Received 7 June 2024; Received in revised form 26 December 2024; Accepted 27 December 2024

Nomenclature

A_h	Cross-section area of the head-side chamber
A_r	Cross-section area of the rod-side chamber
V_h	Volume of the head-side chamber
V_r	Volume of the rod-side chamber
P_h	Pressure in the head-side chamber
P_r	Pressure in the rod-side chamber
P_{hM}	Relief pressure of the head-side relief valve
P_{rM}	Relief pressure of the rod-side relief valve
P_M	Relief pressure of the pump relief valve
Q	Oil flowrate supplied by the pump
p	Position of the actuator rod
v	Velocity of the actuator rod
f	Force generated by the actuator
f_d	Target force for the force controller
M	Mass of the plant
B	Viscosity of the plant
p_0	Position of the environment
K_r	Stiffness of the environment
f_r	Reaction force from the environment
v_x	Velocity of the proxy
M_x	Mass of the proxy
B_x	Viscosity of the proxy
u	Control input, translated into the valve opening ratio
Γ	Map from v and u to f
Θ	Map from v and f to u
Λ	Map from u and f to v
Θ_s	Modified single-valued map from v and f to u
T	Sampling interval of the controller
T_d	Deadtime of the hydraulic system
$\hat{T}_d$	Estimated deadtime used in the stabilizer
β	Bulk modulus of the oil
ρ	Mass density of the oil
C_*	Discharge coefficients of valves†
a_*	Maximum opening areas of valves†
V_R	Stored energy in the plant
V_E	Additional energy due to the deadtime
V_{RE}	Stored energy in the extended system
$\mathcal{X}$	Velocity bound for the stabilizer

†: $*\in\{ph, pr, th, tr, b\}$, which stand for 'pump-to-head', 'pump-to-rod', 'tank-to-head', 'tank-to-rod', and 'bleed', respectively.

without the need for empirical parameter adjustments, but their application has been limited to actuators with simple hydraulic circuits with a few control valves. As far as the authors are aware, there have been no reports of such model-based approaches to more complex hydraulic systems, such as those with multiple relief valves and check valves.

A major problem in the control of hydraulic actuators is deadtime, which is as long as, typically 0.1 s to 0.6 s (Yamamoto et al., 2024, 2021). To handle the deadtime, Kim et al. (2021) proposed a force controller using a neural network, which is trained by time series data of actuators with a deadtime of about 0.08 s. The force controller (Kim et al., 2021) has been reported to perform successfully in high-stiffness environments, but it has not been validated with the actuators with longer deadtime, e.g., 0.1 s to 0.6 s.

This paper proposes a force controller for hydraulic actuators of the valve-manipulated type. Fig. 1(a) shows its overall structure. It has a similar structure to that of an admittance controller, in which a 'proxy', a virtual mass–damper system, converts the measured force signal to a reference (proxy) velocity. In the proposed controller, the force is measured from pressure sensors in the actuator chambers.

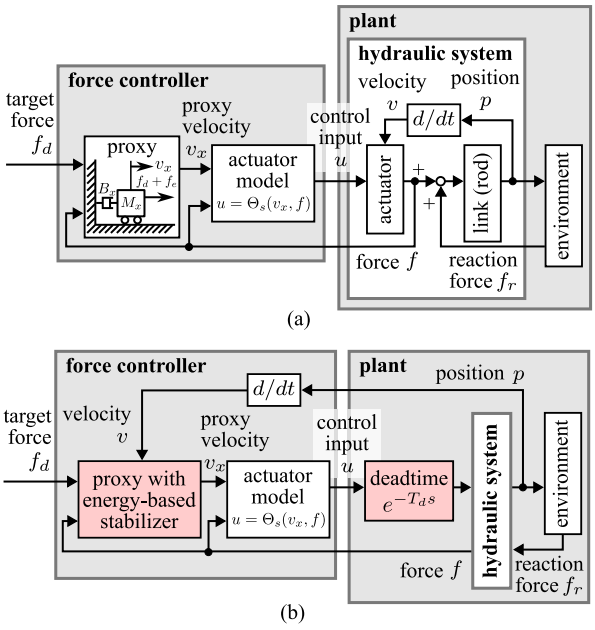

Fig. 1. Hydraulic plant with (a) the proposed force controller and (b) the force controller including the proposed energy-based stabilizer.

The reference velocity is converted into the control input, which is the opening ratio of the main control valves, through Kikuuwe et al. (2021) quasi-static actuator model. In addition, to handle the long deadtime in the hydraulic actuators, this paper also proposes a stabilizer to be embedded in the force controller, as shown in Fig. 1(b). The stabilizer estimates the mechanical energy stored in the whole system, and suppresses the reference velocity so that the stored energy converges to a desired level. The proposed methods were validated with a laboratory hydraulic setup that has the same circuit structure as commercial excavators.

The proposed controller can be seen as advantageous in its structural simplicity, which is described by using only two equations, representing the proxy dynamics and the actuator model (Kikuuwe et al., 2021). Only the mass and viscosity of the proxy need to be adjusted because the actuator model depends solely on parameters derived from available hardware specifications. While the ease of tuning the mass and viscosity parameters is a feature shared with previous admittance control schemes, this controller differs by being free from an internal position controller, which typically requires careful tuning to ensure stability. Furthermore, by being combined with the proposed stabilizer, the controller becomes capable of handling the long deadtime. The effect of the stabilizer was illustrated by some experimental results.

The rest of this paper is organized as follows. Section 2 provides some preliminaries regarding the hydraulic circuit and the quasi-static actuator model (Kikuuwe et al., 2021). Section 3 proposes a force controller and provides its stability analysis. Section 4 proposes an energy-based stabilizer to enhance the stability of the proposed controller under the deadtime. Section 5 presents experimental results of force-tracking tasks by employing a hydraulic setup, which has a hydraulic circuit similar to commercial excavators. Section 6 concludes this paper.

2. Preliminaries

2.1. Mathematical preliminaries

In this paper, $\mathbb{R}$ denotes the set of all real numbers and $\mathcal{B}$ denotes the closed unit ball in $\mathbb{R}$, i.e., $\mathcal{B} \triangleq [-1, 1]$. This paper uses a 'signum' function and a 'projection' function defined as follows:

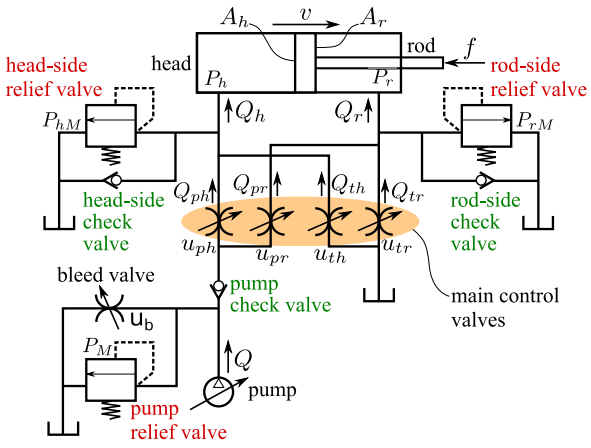

Fig. 2. Hydraulic actuator and its circuit.

$$\mathrm{sgn}(x) \triangleq \begin{cases} x/|x| & \text{if } x \neq 0 \\ [-1,1] & \text{if } x = 0 \end{cases} \tag{1}$$

$$\mathrm{proj}([a,b],x) \triangleq \begin{cases} b & \text{if } x > b \\ x & \text{if } x \in [a,b] \\ a & \text{if } x < a \end{cases} \tag{2}$$

where $a \in \mathbb{R}$, $b \in \mathbb{R}$, $x \in \mathbb{R}$ and $a \leq b$. The function proj returns the closest value of x in the closed interval $[a,b]$. If $a = b$, it always returns a $(= b)$ for any value of x.

2.2. Hydraulic actuator and its circuit

The overall structure of the actuator discussed in this paper is illustrated in Fig. 2. The actuator has a cylinder and a rod, which compose two chambers with cross-sectional areas A_* and internal pressures P_* ($*\in \{h,r\}$ where h means head-side and r means rod-side). To protect the circuit from excessive pressures, the head-side, the rod-side, and the pump relief valves are installed in the circuit, of which the pressure limits are P_{hM}, P_{rM}, and P_M, respectively. In addition, three check valves are installed to prevent the backflow of the oil. Due to the effects of the head-side and rod-side relief valves, the range of the actuator forces is from $-F_{rM} \triangleq -A_r P_{rM}$ to $F_{hM} \triangleq A_h P_{hM}$. The pump supplies the oil flow with a constant flowrate Q.

The ratio of the opening area to its maximum of each of five control valves (four main control valves and the bleed valve) is denoted by $u_* \in [0,1]$ ($*\in \{ph,pr,th,tr,b\}$), where the subscripts indicate which parts the valve connects, e.g., ph indicates that the valve connects the pump and the head-side chamber, and tr indicates that it connects the tank and the rod-side chamber. The control input $u \in \mathcal{B}$ to the actuator is translated into the valve opening ratios of the main control valves in the following rule:

$$u_{ph} = u_{tr} = \max(u,0), \quad u_{pr} = u_{th} = \max(-u,0). \tag{3}$$

This means that when $u > 0$, the valves with u_{ph} and u_{tr} are opened to allow the oil flow in the rod-extending direction, and when $u < 0$, those with u_{pr} and u_{th} are opened for the flow in the rod-contracting direction. The flowrates Q_* of the valves satisfy the following flowrate-pressure relations (Borutzky, Barnard, & Thoma, 2002; Cristofori & Vacca, 2015):

$$Q_* = c_* u_* \,\mathrm{sgn}(\Delta P_*)\sqrt{|\Delta P_*|}, \quad *\in \{ph,tr,th,pr,b\} \tag{4}$$

where $c_* \triangleq C_* a_* \sqrt{2/\rho}$, ΔP_* is the pressure drop across the valve, ρ is the mass density of the oil, a_* is the maximum opening area of the valve, and C_* is its discharge coefficient (Lichtarowicz, Duggins, & Markland, 1965), which is a non-dimensional quantity.

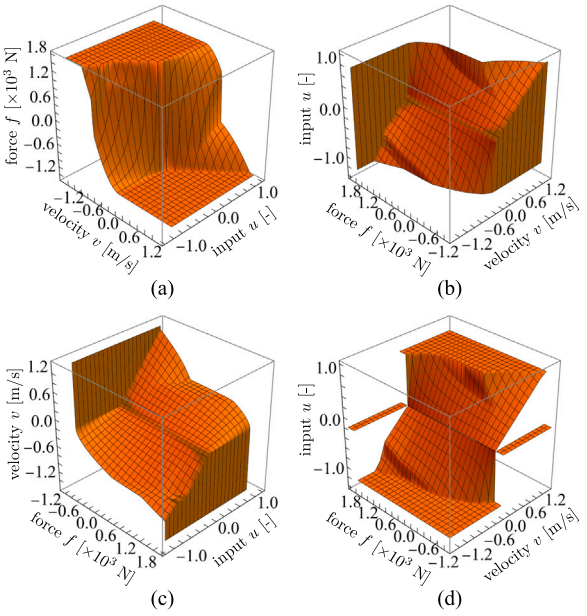

Fig. 3. Graphs representing the actuator model (Kikuuwe et al., 2021; Yamamoto et al., 2021), where u is the control input that determines the opening ratio of the main control valves through (3), f is the actuator force, and v is the actuator velocity. (a) Graph of $f \in \Gamma(v,u)$, (b) Graph of $u \in \Theta(v,f)$, (c) Graph of $v \in \Lambda(u,f)$, and (d) Graph of $u = \Theta_s(v,f)$ in the f-v-u space.

Kikuuwe et al. (2021) proposed a quasi-static model of hydraulic actuators of the structure shown in Fig. 2. The model describes the relations among the rod velocity $v \in \mathbb{R}$, the control input $u \in \mathcal{B}$, and the force f under the quasi-static condition. The relations are described in the following:

$$f \in \Gamma(v,u) \iff u \in \Theta(v,f) \iff v \in \Lambda(u,f) \tag{5}$$

where Γ, Θ, and Λ are set-valued functions. Fig. 3(a)(b)(c) show the graphs of the functions Γ, Θ, and Λ, respectively, with the parameters of the experimental setup introduced in Section 5.1. In these graphs, the set-valuedness appears as vertical walls or lines. The vertical walls in the graphs of Θ and Λ, which are orthogonal to the f axis, represent the force saturation caused by the relief valves. The exact analytical forms of the set-valued functions Γ and Θ are presented in Yamamoto et al. (2021, Section III.A). Because they are quite lengthy, they are omitted in this paper for brevity.

Set-valued functions such as Θ are not feasible for implementation in controller algorithms because a single value must always be selected at every computational step in algorithms. For the use of Θ in controller algorithms, the authors' previous paper (Yamamoto et al., 2021) introduced a single-valued function Θ_s that satisfies the following:

$$\Theta_s(v,f) \in \Theta\left(v, \mathrm{proj}(\Gamma(v,\mathcal{B}),f)\right). \tag{6}$$

The function Θ_s has been constructed considering various implementation constraints, and its exact analytical form is provided in Yamamoto et al. (2021, Section III.B). Due to the length of the expression, it is also omitted here for brevity. Fig. 3(d) shows the graph of the function Θ_s using the parameters of the experimental setup introduced in Section 5.1. As can be seen in Fig. 3(d), the function Θ_s sets the control input u to be a saturated value when the velocity v is large, and to be zero when the force f exceeds the relief-valve limits in the opposite direction of v. The function Θ_s has already been utilized in another previous paper (Yamamoto et al., 2024) of the authors.

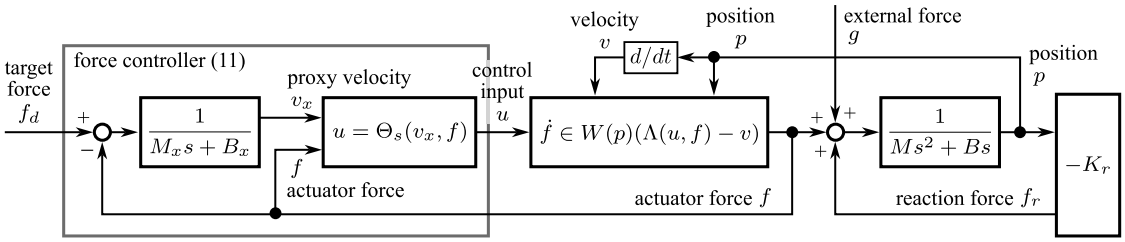

Fig. 4. Block diagram of the proposed controller (11) applied to the plant (10).

2.3. Plant model

This paper extends the quasi-static model to handle the pressure dynamics of the complex hydraulic circuit. Assuming that inner leakage between the chambers is sufficiently small, the pressure dynamics (Akers, Gassman, & Smith, 2006, Chapter 4.3.1) in the head- and rod-side chambers can be written as follows:

$$\dot{P}_h = \frac{\beta}{V_h(p)}\left(Q_h - A_h v\right) \tag{7a}$$

$$\dot{P}_r = \frac{\beta}{V_r(p)}\left(Q_r + A_r v\right) \tag{7b}$$

where β is the oil bulk modulus, and Q_h and Q_r are the flowrates into the head- and rod-side chambers, respectively. The volumes of the head- and rod-side chambers, denoted by $V_h(p) > 0$ and $V_r(p) > 0$, respectively, depend on the rod position $p \in [p_{\min}, p_{\max}]$.

The flowrates Q_h and Q_r are given from the function Λ in (5) as follows:

$$Q_h \in A_h \Lambda(u, f) \tag{8a}$$

$$Q_r \in -A_r \Lambda(u, f). \tag{8b}$$

Substituting (8) into (7), one can obtain the dynamics of the actuator force $\dot{f} = A_h \dot{P}_h - A_r \dot{P}_r$ as follows:

$$\dot{f} \in W(p)\left(\Lambda(u, f) - v\right) \tag{9}$$

where $W(p) \triangleq \beta(A_h^2/V_h(p) + A_r^2/V_r(p)) > 0$.

It should be noted that the model (9) has a similar structure to some previous models, such as those in Ruderman et al. (2019) and Ruderman (2017). Specifically, the model (9) includes the effects of all valves in the circuit of Fig. 2 by the inclusion of the set-valued function Λ, while it neglects the dynamics of the spool valve, which is often modeled as a second-order system (Ruderman, 2017; Ruderman et al., 2019).

Remark 1. Theoretical properties of the function $\Gamma(v, u)$ have been detailed in the authors' previous paper (Kikuuwe, Yamamoto, & Brogliato, 2022, Section III), from which properties of the function $\Lambda(v, f)$ can also be deduced. One can see that the right-hand side of the differential inclusion (9), involving $\Lambda(v, f)$, is closed and convex, is outer semicontinuous (cf. Hiriart-Urruty and Lemaréchal (2001, p. 14)) with respect to f, and is maximal monotone (cf. Acary & Brogliato, 2008, Section 2.1.2) with respect to $-f$. According to Smirnov (2002, Theorem 4.7) and Acary and Brogliato (2008, Theorem 2.41), one can conclude that the differential inclusion (9) has a unique solution from any initial value.

3. Proposed controller

3.1. Force controller

The proposed force controller is intended to be applied to the following hydraulic plant:

$$\dot{f} \in W(p)\left(\Lambda(u, f) - \dot{p}\right) \tag{10a}$$

$$M\ddot{p} + B\dot{p} = f + f_r + g \tag{10b}$$

where $p \in \mathbb{R}$ and $M > 0$ denote the position and mass, respectively, of the controlled object, which is subjected to the external force g, the actuator force f, and the reaction force f_r from the environment. The actuator force f is given by (10a) including the set-valued function Λ, which is introduced in Section 2.3.

This paper presents the following controller:

$$M_x \dot{v}_x + B_x v_x = f_d - f \tag{11a}$$

$$u = \Theta_s(v_x, f) \tag{11b}$$

where v_x denotes the velocity of the 'proxy', M_x and B_x are the mass and the viscosity of the proxy, respectively, and f_d is the target force. Note that the function Θ_s, which has been introduced in (6), is a single-valued function. It is assumed that the actuator force f is measured by pressure sensors in the actuator chambers. Fig. 4 shows the block diagram of the proposed controller (11) applied to the plant (10).

A discrete-time algorithm of the controller (11) can be derived through the implicit Euler method. The implicit Euler discretization of (11) can be obtained as follows:

$$f_{d,k} - f_k = M_x \frac{v_{x,k} - v_{x,k-1}}{T} + B_x v_{x,k} \tag{12a}$$

$$u_k = \Theta_s(v_{x,k}, f_k) \tag{12b}$$

where T is the sampling interval of the controller and k is the index of the discrete time. Considering that (12a) should be used to obtain the proxy velocity $v_{x,k}$ of the current control cycle k, the discrete-time algorithm for the controller can be derived as follows:

$$v_{x,k} := \frac{M_x v_{x,k-1} + (f_{d,k} - f_k)T}{M_x + B_x T} \tag{13a}$$

$$u_k := \Theta_s(v_{x,k}, f_k). \tag{13b}$$

3.2. Stability analysis

The stability properties of the proposed controller (11) are now analyzed to provide baseline guarantees for the controller. The situation discussed here involves the plant (10) being in contact with an elastic environment that can be described in the following form:

$$f_r = -K_r(p - p_0) \tag{14}$$

where p_0 and K_r are the position and the stiffness of the environment, respectively. Then, the plant (10) combined with the environment (14) and the controller (11) can be represented in the following state-space form:

$$\dot{\boldsymbol{x}} \in \boldsymbol{A}_r(p)\boldsymbol{x} + \boldsymbol{B}\boldsymbol{g} + \boldsymbol{e}W(p)\Lambda(\Theta_s(v_x, f), f) \tag{15a}$$

where

$$\boldsymbol{x} \triangleq [f - f_d, v_x, v, p - p_o - f_d/K_r]^T \in \mathbb{R}^4 \tag{15b}$$

$$\boldsymbol{A}_r(p) \triangleq \begin{bmatrix} 0 & 0 & -W(p) & 0 \\ -1/M_x & -B_x/M_x & 0 & 0 \\ 1/M & 0 & -B/M & -K_r/M \\ 0 & 0 & 1 & 0 \end{bmatrix} \in \mathbb{R}^{4\times 4} \tag{15c}$$

$$\boldsymbol{B} \triangleq \begin{bmatrix} -1 & 0 \\ 0 & 0 \\ 0 & 1/M \\ -1/K_r & 0 \end{bmatrix} \in \mathbb{R}^{4\times 2} \tag{15d}$$

$$\boldsymbol{g} \triangleq [\dot{f}_d, g]^T \in \mathbb{R}^2 \tag{15e}$$

$$\boldsymbol{e} \triangleq [1,0,0,0]^T \in \mathbb{R}^4. \tag{15f}$$

The functions Λ and Θ_s represent the quasi-static actuator model (Kikuuwe et al., 2021), introduced in Section 2.2. As can be seen in Fig. 3, as long as the actuator force f is not saturated, Λ is single-valued and Θ_s is continuous. Consequently, when the force f is not saturated, the right-hand side of (15a) is single-valued and continuous and thus the system (15) can be viewed as an ordinary differential equation, allowing for discussions on its equilibria.

It should also be noted that the expression (15) holds true even in the case where $f_d \equiv 0$ and $K_r = 0$, i.e., where the target force is set to zero and the plant is not in contact with the environment. In such a case, the fourth component of the state vector $\boldsymbol{x}$ should be set to $p - p_o$, where p_o can be an arbitrary constant.

In the system (15a), the function Λ is in the plant and the function Θ_s is the plant model used in the controller. As long as the model Θ_s is accurately related to Λ and the arguments f and u are unsaturated, the relation $\Lambda(\Theta_s(v_x, f), f) = v_x$ holds. Considering the inaccuracy of the model Θ_s and the possibility of the saturations in f and u, one can write

$$\Lambda(\Theta_s(v_x, f), f) = v_x + \tilde{v}_x \tag{16}$$

where $\tilde{v}_x$ can be understood as the disturbance that can be caused by the modeling error and the saturations in f and u. Then, the system (15) can be rewritten in the following form:

$$\dot{\boldsymbol{x}} = \boldsymbol{A}(p)\boldsymbol{x} + \boldsymbol{B}\boldsymbol{g} + \boldsymbol{e}W(p)\tilde{v}_x \tag{17a}$$

where

$$\boldsymbol{A}(p) \triangleq \begin{bmatrix} 0 & W(p) & -W(p) & 0 \\ -1/M_x & -B_x/M_x & 0 & 0 \\ 1/M & 0 & -B/M & -K_r/M \\ 0 & 0 & 1 & 0 \end{bmatrix}. \tag{17b}$$

The difference between the matrices $\boldsymbol{A}_r(p)$ and $\boldsymbol{A}(p)$ is that (1,2)th element is altered from 0 to $W(p)$. Here, note that, as long as the force f is not saturated, the system (15) is reduced to the linear parameter-varying (LPV) system (17), which does not involve the set-valuedness any longer.

Hereafter, the equilibria of the LPV system (17), characterized by the matrices $\boldsymbol{A}(p)$ and $\boldsymbol{B}$, are discussed in two cases: the case of $K_r = 0 \wedge f_d \equiv 0$, where the system is not in contact with an environment, and the case of $K_r > 0$, where it is in contact with an environment. First, let the following subset of the state space be defined:

$$\mathcal{S} \triangleq \left\{ [0,0,0,\tilde{p}]^T \in \mathbb{R}^4 \mid \tilde{p} \in \mathbb{R} \right\}. \tag{18}$$

The matrix $\boldsymbol{A}(p)$ is full rank if $K_r > 0$, but it has the null space $\mathcal{S}$ if $K_r = 0$. Therefore, the origin $\boldsymbol{0}$ is the equilibrium of the system if $K_r > 0$, and all states included in $\mathcal{S}$ are equilibria if $K_r = 0$ and $f_d = 0$. It means that, if the system is in contact with an environment and $f_d > 0$, it is in equilibrium at the position $p = p_o + f_d/K_r$. Meanwhile, if the system is not in contact with an environment and $f_d = 0$, it is in equilibrium at any positions p.

The stability of the equilibria is now discussed. In the nonlinear system (17), the position p depends on the fourth component of the state vector $\boldsymbol{x}$ and the matrix $\boldsymbol{A}(p)$ depends on the position p. Therefore, the stability of an equilibrium $\boldsymbol{x}_s$, satisfying $\boldsymbol{A}(p)\boldsymbol{x}_s = \boldsymbol{0}$, can be examined through the following Jacobian matrix:

$$\begin{aligned} \left.\frac{\partial(\boldsymbol{A}(p)\boldsymbol{x})}{\partial \boldsymbol{x}}\right|_{\boldsymbol{x}=\boldsymbol{x}_s} &= \boldsymbol{A}(p) + \left.\frac{\partial(\boldsymbol{A}(p)\boldsymbol{x}_c)}{\partial \boldsymbol{x}}\right|_{\boldsymbol{x}=\boldsymbol{x}_c=\boldsymbol{x}_s} \\ &= \boldsymbol{A}(p) + \left.\begin{bmatrix} \boldsymbol{0}^{4\times 3} & W'(p)(v_x - v) \\ & \boldsymbol{0}^{3\times 1} \end{bmatrix}\right|_{v_x=v=0} \\ &= \boldsymbol{A}(p) \end{aligned} \tag{19}$$

where $\boldsymbol{0}^{m\times n}$ denotes the $m \times n$ zero matrix. The fact that $v_x = v = 0$ in equilibrium in both cases of $K_r = 0$ and $K_r > 0$ is used here. The above derivation shows that the matrix $\boldsymbol{A}(p)$ itself is the Jacobian matrix of the system (17) at the origin if $K_r > 0$ and at any points in $\mathcal{S}$ if $K_r = 0$.

It is now possible to observe a result regarding the situation where the plant is not in contact with an environment, i.e., $f_d \equiv 0$ and $K_r = 0$. The following result implies that the system with $f_d \equiv 0$ can be in stable equilibrium at any positions:

Theorem 1. *With the system (17) satisfying $M_x > 0$, $B_x > 0$, $K_r = 0$, $f_d \equiv 0$, $\boldsymbol{g} \equiv \boldsymbol{0}$, and $\tilde{v}_x \equiv 0$, the subset $\mathcal{S}$ is asymptotically stable.*

Proof. Let $\boldsymbol{A}_b(p) \in \mathbb{R}^{3\times 3}$ be the upper-left 3×3 block of the matrix $\boldsymbol{A}(p)$ and $\boldsymbol{x}_b \in \mathbb{R}^3$ be the vector composed of upper three components of $\boldsymbol{x}$. From $K_r = 0$, $f_d \equiv 0$, $\boldsymbol{g} \equiv 0$, and $\tilde{v}_x \equiv 0$, the LPV system (17) can be written as follows:

$$\begin{bmatrix} \dot{\boldsymbol{x}}_b \\ \dot{p} \end{bmatrix} = \begin{bmatrix} \boldsymbol{A}_b(p)\boldsymbol{x}_b \\ v \end{bmatrix}. \tag{20}$$

Then, it is easy to see that $\boldsymbol{A}_b(p)$ is Hurwitz. Therefore, for a positive definite matrix $\boldsymbol{Q}_b \in \mathbb{R}^{3\times 3}$, there exists a positive definite matrix $\boldsymbol{P}_b(p) \in \mathbb{R}^{3\times 3}$ satisfying

$$\boldsymbol{P}_b(p)\boldsymbol{A}_b(p) + \boldsymbol{A}_b(p)^T\boldsymbol{P}_b(p) = -\boldsymbol{Q}_b. \tag{21}$$

A Lyapunov function candidate V_b is defined as

$$V_b(\boldsymbol{x}) \triangleq \frac{1}{2}\boldsymbol{x}^T \begin{bmatrix} \boldsymbol{P}_b(p) & 0 \\ 0 & 0 \end{bmatrix} \boldsymbol{x} = \frac{\boldsymbol{x}_b^T\boldsymbol{P}_b(p)\boldsymbol{x}_b}{2}. \tag{22}$$

Then, it satisfies $V_b(\boldsymbol{x}) = 0$ for all $x \in \mathcal{S}$ and $V_b(\boldsymbol{x}) > 0$ for all $x \notin \mathcal{S}$. Because of $K_r = 0$, it also satisfies the following:

$$\begin{aligned} \dot{V}_b(\boldsymbol{x}) &= -\boldsymbol{x}^T \begin{bmatrix} \boldsymbol{Q}_b & 0 \\ 0 & 0 \end{bmatrix} \boldsymbol{x} + \boldsymbol{x}^T \begin{bmatrix} 2v\dfrac{\partial \boldsymbol{P}_b(p)}{\partial p} & 0 \\ 0 & 0 \end{bmatrix} \boldsymbol{x} \\ &\le -\|\boldsymbol{x}_b\|^2\lambda_Q + \|\boldsymbol{x}_b\|^2\gamma_R(p)|v| \\ &= -\|\boldsymbol{x}_b\|^2(\lambda_Q - \gamma_R(p)|v|) \end{aligned} \tag{23}$$

where λ_Q is the minimum eigenvalue of $\boldsymbol{Q}_b$ and $\gamma_R(p)$ is the maximum of the absolute values of the eigenvalues of $2\partial\boldsymbol{P}_b(p)/\partial p$. Because there always exist v satisfying $|v| < \lambda_Q/\gamma_R(p)$, there always exists a neighborhood of $\mathcal{S}$ in which $\dot{V}_b(\boldsymbol{x}) < 0$ is satisfied. Needless to say, it also satisfies $\dot{V}_b(\boldsymbol{x}) = 0$ for all $x \in \mathcal{S}$. Therefore, the subset $\mathcal{S}$ is asymptotically stable. □

It is also possible to observe a result regarding the system in contact with an environment. The following result implies that the system is in stable equilibrium at the position $p = p_o + f_d/K_r$ if it is in contact with an environment with the stiffness $K_r > 0$:

Theorem 2. *With the system (17) satisfying $M_x > 0$, $B_x > 0$, $K_r > 0$, $\boldsymbol{g} \equiv \boldsymbol{0}$, and $\tilde{v}_x \equiv 0$, the origin $\boldsymbol{0}$ is asymptotically stable (a) if $M_x > M$, (b) if B_x is sufficiently large, or (c) $B = 0$.*

Proof. Because the system (17) is an autonomous system, its origin is asymptotically stable if the Jacobian matrix of the system at the origin is Khalil (2002, Theorem 4.7). The Jacobian matrix is, as suggested in (19), obtained as $\boldsymbol{A}_o \triangleq \boldsymbol{A}(p_o + f_d/K_r)$ since the origin corresponds to $p = p_o + f_d/K_r$. From the characteristic polynomial of $\boldsymbol{A}_0$ and from Routh–Hurwitz stability criterion, one can see that $\boldsymbol{A}_0$ is Hurwitz if the following condition is satisfied:

$$\begin{aligned} &W_0^2(B + B_x)\left(BM_x^2 + B_xM^2\right) + \\ &\quad W_0BB_x\left(B^2M_x + BB_x(M + M_x) + B_x^2M + 2K_rM_x(M_x - M)\right) + \\ &\qquad BB_xK_r\left(BB_xM_x + B_x^2M + K_rM_x^2\right) > 0 \end{aligned} \tag{24}$$

where $W_0 \triangleq W(p_0+f_d/K_r)$. It can be easily seen that (24) holds true (a) if $M_x > M$, (b) if B_x is sufficiently large (e.g., large enough to satisfy $B_x^2 > 2K_rM_x$), or (c) $B = 0$. □

Some remarks related to Theorems 1 and 2 are as follows:

Remark 2. Theorems 1 and 2, demonstrating the asymptotic stability of the origin under zero disturbance, imply the existence of a Lyapunov function. Therefore, one can see that the state converges to a neighborhood of the origin of the state space if the disturbance $[\dot{f}_d, g, \tilde{v}_x]^T$ is bounded to be small enough. This means that the controller can tolerate a certain level of modeling error in Θ, although its tolerance limit is not clarified here.

Remark 3. The disturbance $\tilde{v}$ can be induced by the saturations in the force f and the control input u. The f-saturation happens when one of the relief valves opens by a large external load. The u-saturation happens when the control input u reaches either 1 or -1 as the result of a large proxy velocity v_x. The f-saturation may also cause a discontinuity in u. Theorems 1 and 2 exclude such cases by the assumption that $\tilde{v}$ is small enough. This assumption can be usually maintained by setting the target force f_d within the relief-valve limits and heightening the proxy parameters M_x and B_x.

Remark 4. In a strict sense, Theorem 2 supports the use of the controller only as a force set-point controller because the rate-of-change $\dot{f}_d$ of the target force is treated as a part of the disturbance. If it is used as a force-tracking controller with time-varying f_d, there must be a limitation on the bandwidth, which has not been clarified here. It has been pointed out (Alleyne & Liu, 1999; Dyke, Spencer, Quast, & Sain, 1995) that force-control systems inherently face bandwidth limitations due to the environment interconnected with the actuator, which is also the case in the system (17).

Remark 5. When the environment is damped, i.e., when (14) has additional damping term $-B_r\dot{p}$ in the right-hand side where $B_r > 0$, the coefficient B in the state-space representations (15) and (17) should be understood as the sum of viscosities of the plant and the environment. That is, the environment damping only increases B in (15) and (17). Therefore, Theorem 2 holds even under the damped environment. Whether the increase of B (due to the damped environment) has a positive or negative effect on the stability is determined by the condition (24), depending on other system parameters. Aside from stability issues, a positive effect of the environment damping on the force tracking bandwidth has been discussed in Alleyne and Liu (1999).

Remark 6. The analysis in this section does not account for the deadtime in the plant, but one can infer that increasing the left-hand side of the inequality (24) usually results in a larger phase margin, resulting in a higher robustness to the deadtime. Actually, if there exists a deadtime in the plant, v_x in the third term of the right-hand side of (15a) should be replaced by $v_{xT} \triangleq v_x(t-T_d)$, which is the delayed v_x. Then, the transfer function from v_{xT} to v_x through the system (15) can be written as $\mathcal{L}[v_x]/\mathcal{L}[v_{xT}] = -e^{-T_d s}G(s)$ where

$$G(s) \triangleq \frac{W_0(Ms^2+Bs+K_r)}{s(M_xs+B_x)(Ms^2+Bs+K_r+W_0)}. \tag{25}$$

A stability analysis involving the deadtime may be possible through the Nyquist plot of $e^{-T_d s}G(s)$, though it would require assumptions on plant parameter values. A method for preventing the instability caused by the deadtime is presented in the next section.

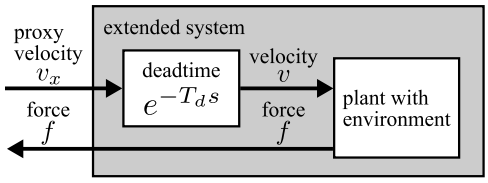

Fig. 5. Extended System, of which input is the proxy velocity v_x and output is the actuator force f.

4. Energy-based stabilizer

The problem of the controller (13) built upon the plant model (10) is that it does not consider the plant deadtime, which is quite common in hydraulic systems. More specifically, the control command u_k sent to the actuator will take some time to take effect as u in the plant (10). This deadtime causes instability, resulting in the divergence of the system energy. To suppress the instability, a method is proposed here to limit the reference velocity v_x, thereby maintaining the system energy at a desired level.

The case where the plant (10) is in contact with the elastic environment (14) is now discussed. It can be seen as a system with the following storage function:

$$V_R \triangleq \frac{K_r(p-p_0)^2}{2} + \frac{Mv^2}{2} = \frac{f^2}{2K_r} + \frac{Mv^2}{2}. \tag{26}$$

One can also consider an extended system involving the deadtime T_d with the input v_x and the output as illustrated in Fig. 5. Let the following energy function be defined:

$$V_E \triangleq \int_{t-T_d}^{t} v_x(\tau)f(\tau)d\tau. \tag{27}$$

Then, one can assume that the stored energy in the extended system can be given as follows:

$$V_{RE} \triangleq V_R + V_E \tag{28a}$$

$$= \frac{f^2}{2K_r} + \frac{Mv^2}{2} + \int_{t-T_d}^{t} v_x(\tau)f(\tau)d\tau. \tag{28b}$$

Let a target energy V_D be defined as $V_D = fd^2/(2Kr)$. Then, realizing $V_{RE} \to V_D$ and $v_x \to 0$ results in $f \to f_d$ and $v \to 0$. The reference velocity v_k, which is originally determined as (13a), should be modified to shift V_{RE} closer to V_D as long as the modified v_x is not farther from 0 than v_x. The current value of $V_{RE,k}$ can be determined by $v_{x,k}$ as follows:

$$V_{RE,k} = V^*_{RE,k} + Tf_kv_{x,k} \tag{29}$$

where

$$V^*_{RE,k} \triangleq \frac{f_k^2}{2K_r} + \frac{Mv_k^2}{2} + \sum_{i=1}^{\mathrm{floor}(T_d/T)} Tf_{k-i}v_{x,k-i} \tag{30}$$

and the function floor returns the greatest integer less than or equal to its argument. Therefore, to set $V_{RE,k}$ closer to V_D in comparison to $V^*_{RE,k}$, the proxy velocity v_x should be chosen to satisfy the following:

$$(V_D - V^*_{RE,k})(V_{RE,k} - V^*_{RE,k}) \geq 0, \tag{31}$$

which is equivalent to

$$(V_D - V^*_{RE,k})f_kv_{x,k} \geq 0. \tag{32}$$

This means that the proxy velocity $v_{x,k}$, which is originally set as (13a), should be set as

$$v_{x,k} = \mathrm{proj}\left(\mathcal{X}, \frac{M_xv_{x,k-1} + (f_{d,k} - f_k)T}{M_x + B_xT}\right) \tag{33}$$

where

$$\mathcal{X} = \begin{cases} [0,\infty) & \text{if } (V_{D,k} - V^*_{RE,k})f_k \geq 0 \\ (-\infty, 0] & \text{otherwise.} \end{cases} \tag{34}$$

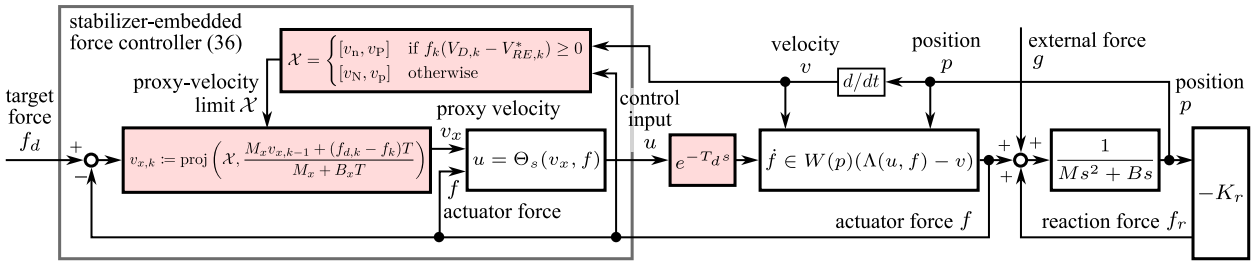

Fig. 6. Block diagram of the stabilizer-embedded controller (36) applied to the plant (10) with the deadtime T_d. In this block diagram, the proxy and the stabilizer are represented in their discretized form.

In reality, the stiffness K_r and the mass M should be replaced by their estimated values, but there must be inevitable errors in such values, which would cause errors in V_D and V^*_{RE}. The proxy-velocity limit (34) may result in the proxy stuck at an unintended state, which would cause the steady-state error in the force f from the target force f_d. To avoid this, the constraint (34) should be relaxed so that a small proxy velocity $v_x \in [v_n, v_p]$ (where $v_n < 0 < v_p$) is always allowed. In addition, the proxy velocity should be prevented from becoming excessively large, by being bounded by $[v_N, v_P]$, where $v_N \ll v_n < 0 < v_p \ll v_P$. Considering in this way, one can relax the constraint (34) as follows:

$$\mathcal{X} = \begin{cases} [v_n, v_P] & \text{if } (V_{D,k} - V^*_{RE,k}) f_k \geq 0 \\ [v_N, v_p] & \text{otherwise,} \end{cases} \tag{35}$$

Hereafter, Eq. (33), projecting the proxy velocity v_x to the energy-based limit (35), is referred to as an "energy-based stabilizer".

Thus, the controller algorithm (13) combined with the energy-based stabilizer (33) can be given as follows:

$$V^*_{RE,k} := \frac{f_k^2}{2\hat{K}_r} + \frac{\hat{M} v_k^2}{2} + \sum_{i=1}^{\mathrm{floor}(T_d/T)} T f_{k-i} v_{x,k-i} \tag{36a}$$

$$V_{D,k} := \frac{f_{d,k}^2}{2\hat{K}_r} \tag{36b}$$

$$\mathcal{X} := \begin{cases} [v_n, v_P] & \text{if } (V_{D,k} - V^*_{RE,k}) f_k \geq 0 \\ [v_N, v_p] & \text{otherwise,} \end{cases} \tag{36c}$$

$$v_{x,k} := \mathrm{proj}\left(\mathcal{X}, \frac{M_x v_{x,k-1} + (f_{d,k} - f_k)T}{M_x + B_x T}\right) \tag{36d}$$

$$u_k := \Theta_s(v_{x,k}, f_k) \tag{36e}$$

where $\hat{K}_r$, $\hat{M}$, and $\hat{T}_d$ are the estimated values of the environment stiffness, the plant mass, and the deadtime, respectively. The inputs to the algorithm are the measured force f_k, the target force $f_{d,k}$, and the measured velocity v_k, and the output from the algorithm is the control input u_k. The values of f_{k-i} and $v_{x,k-i}$, $i \in \{1, \ldots, \mathrm{floor}(T_d/T)\}$, should be stored in the controller. Note that, again, the function Θ_s in (36e) is a single-valued function introduced in (6), which can be directly used in an algorithm. The block diagram of the stabilizer-embedded controller (36) is shown in Fig. 6.

In practical cases, it is not always possible to obtain an accurate value for the deadtime. It can be inferred that, if $\hat{T}_d > T_d$, the proxy velocity will be unnecessarily suppressed, and thus the system tends to become stable, although slow in its response. In practice, it would be safer to use a slightly larger value for $\hat{T}_d$ and then reduce it until a sufficient response is obtained without instability.

A strict stability analysis involving the stabilizer is still an open problem. One possible justification follows. When there is a deadtime, v_x in the third term of the right-hand side of (15a) should be replaced by $v_{xT} \triangleq v_x(t - T_d)$, which is the delayed v_x. Then, the transfer function from v_{xT} to v_x through the system (15) can be written as $\mathcal{L}[v_x]/\mathcal{L}[v_{xT}] = -e^{-T_d s} G(s)$ where $G(s)$ is defined by (25). One can see that setting B_x higher results in a larger phase margin of the transfer function $G(s)$, leading to higher robustness against the deadtime. The effect of the stabilizer is to reduce $|v_x|$, which is equivalent to setting a higher value (than the actual value) for the proxy viscosity B_x at every sampling step. Thus, one can infer that the stabilizer at least has a positive effect on stability, although it is not a guarantee.

Table 1
Parameters of the hydraulic actuator. (For the meanings of the symbols, see the Nomenclature.)

symbols	values
Q	4.17×10^{-4} m^3/s
A_h	8.04×10^{-4} m^2
A_r	5.50×10^{-4} m^2
P_{hM}, P_{rM}, P_M	2.0 MPa
u_b	0.1
a_* $(*\in \{ph, tr, th, pr\})$	1.9×10^{-5} m^2
a_b	8.2×10^{-6} m^2
C_* $(*\in \{ph, tr, th, pr, b\})$	0.6
ρ	880 kg/m^3

5. Experiments

5.1. Setup

The proposed controller was tested with a hydraulic actuator driven by the hydraulic circuit shown in Fig. 2. The setup is shown in Fig. 7. A proportional valve EHDFG-03-60-3C2-XY-30 (Yuken Kogyo Co., Ltd.) was used as the main control valve, which proportionally changed the valve opening ratio following the received voltage. The oil flow was supplied from the pump unit YAL16-B-2-2.2-20 (Yuken Kogyo Co., Ltd.), which generated a constant flowrate Q. The parameters of the hydraulic circuit and actuator are shown in Table 1.

As shown in Fig. 7, the setup included a contact environment composed of a Shore-A50 rubber block of the thickness 20 mm and a steel plate of the thickness 5 mm placed between the actuator rod and the rubber block. When the actuator rod contacts with the environment, the steel plate is displaced, compressing the rubber block. It was used to avoid complications that may be caused by surface deformation of the rubber block when it was in direct contact with the rod. The rod mass was 1 kg and a 5 kg weight was connected to the rod, i.e., the total mass of the moving parts was 6 kg.

The actuator position p was measured by an incremental linear encoder MLS-30-4500-500 (Microtech Laboratory Inc.), of which the resolution was 5×10^{-3} mm. The head-side pressure P_h and the rod-side pressure P_r were measured with pressure sensors EH15-874-P4R70C0 (Nagano Keiki Co., Ltd.) and were used to obtain the actuator force $f = P_h A_h - P_r A_r$. The controller was implemented in a Windows PC using the Microsoft Visual C++ developing environment. The sampling interval was set as $T = 0.01$ s.

The parameters of the proposed force controller were set as $M_x = 8$ kg and $B_x = 1.0 \times 10^4$ N s/m. The function Θ_s in the proposed controller (13) was built using the parameter values listed in Table 1. The parameter values in Table 1 were set according to the specification

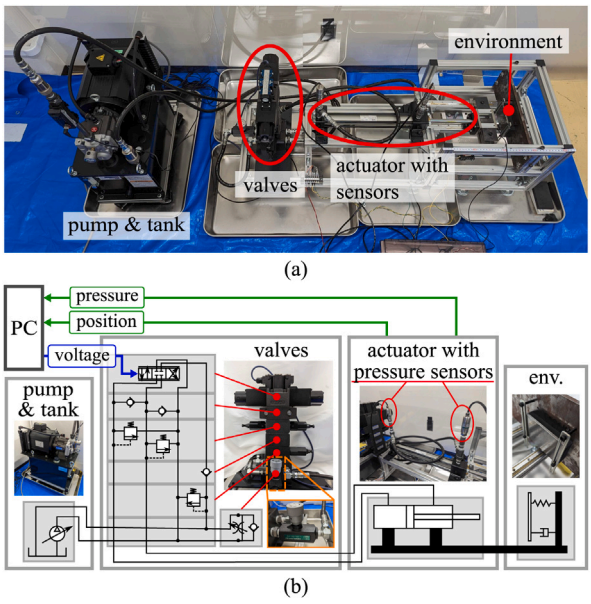

Fig. 7. Hydraulic setup. (a) Overview. (b) Overall diagram.

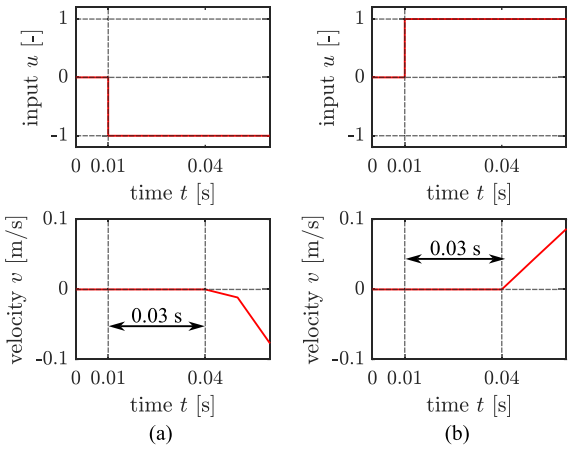

Fig. 8. Results of preliminary experiments: (a) the deadtime observed at the onset of rod extension, (b) the deadtime observed at the onset of rod retraction.

documents of the pump, the valves, the cylinder, and the oil provided by their manufacturers. As for the stabilizer-embedded controller (36), the proxy-velocity limits were set as $v_N = -2.5 \times 10^{-2}$ m/s, $v_n = -1.0 \times 10^{-4}$ m/s, $v_p = 5.0 \times 10^{-4}$ m/s, and $v_P = 2.0 \times 10^{-2}$ m/s. The stiffness $\hat{K}_r$ and the mass $\hat{M}$ were set as 5.0×10^5 N/m and 6 kg, respectively. This stiffness $\hat{K}_r$ was calculated from the displacement-to-force ratio of the rubber block obtained through some simple measurements, and the mass $\hat{M}$ was set as the total mass of the moving parts.

5.2. Preliminary experiments: Deadtime

To check the deadtime at the beginning of the actuator motion, the initial step responses were recorded with two motions. The experimental results are shown in Fig. 8(a) and (b). In Fig. 8(a), the control input u was set as -1, which means that the control valves were fully opened to shorten the rod position p, and measured its velocity v. As seen from the velocity v in Fig. 8(a), the deadtime was about 0.03 s, which was three times the sampling interval T of the controller. In Fig. 8(b), the control input u was set as 1, which means that the control valves were fully opened to extend the rod position p. As in this case, the deadtime was also about 0.03 s.

It should be noted that the deadtime in the laboratory setup is significantly shorter than the typical deadtime found in commercially available hydraulic excavators, which ranges from approximately 0.1 s to 0.6 s (Yamamoto et al., 2024, 2021). To investigate the applicability of the proposed method to hydraulic construction machinery, in the experiments of Sections 5.4 to 5.6, a software-emulated deadtime was inserted before sending the command u to the actuator.

5.3. Experiment I : Force controller

Some experiments were conducted to validate the proposed force controller (13), without the stabilizer, with two different environments, which are a rubber block and a steel plate. In all experiments, the force controller was activated as $t = 2$ s, and the target force f_d was changed in a step-like manner.

Fig. 9(a) and (b) show the experimental results with the rubber block and the steel plate, respectively. As seen in these results, the actuator force f converged to the target force f_d for both environments. It should be noted that the parameter values were the same across environments with different contact stiffness. The difference in stiffness can be seen in the different magnitudes of variations in the position p in Fig. 9(a) and (b); it varied in the range of approximately 1.0 mm with the rubber block, while 0.5 mm with the steel plate.

It should also be noted that the controller (13) used here did not involve any explicit countermeasures for the deadtime, which was $T_d = 0.03$ s in this setup as mentioned in Section 5.2. These results show a certain level of the robustness of the controller (13) against unmodeled factors of the plant. In the results in Fig. 9, the settling time of the step response appears to be between 0.5 s and 1.0 s in both environments. This value is much larger than the time constant of decay of the second-order system $1/(M_x s^2 + B_x s + \hat{K}_r)$ with the parameter values given in Section 5.1, which is around 0.02 s. Therefore, the plant deadtime of $T_d = 0.03$ s seems to play a significant role in determining the bandwidth of the controller.

5.4. Experiment II : Effects of proxy viscosity

It has been known that the instability can be alleviated by increasing the proxy viscosity in admittance-controlled systems (Ferraguti et al., 2019; Haninger et al., 2022; Kikuuwe, 2019; Liu et al., 2022). Some experiments were performed to test whether this is also the case with the proposed controller (13). Specifically, a software deadtime, which makes the system prone to instability, was inserted as mentioned in Section 5.2, and the effects of different proxy viscosities B_x were investigated.

Fig. 10(a) shows the experimental results with the deadtime $T_d = 0.3$ s. From the comparison among the results shown in Fig. 10(a), setting a large value to the proxy viscosity B_x results in the force f converging to the target force f_d without large oscillations. It shows that, setting $B_x = 5.0 \times 10^4$ N s results in a desirable response with small oscillations and quick responses, plotted in (blue), even under the deadtime of $T_d = 0.3$ s. In contrast, Fig. 10(b) shows that with $T_d = 0.6$ s, it became more difficult to achieve desirable responses only by the tuning of the viscosity B_x.

These results suggest that, with the controller (13), increasing the proxy viscosity B_x enhances the stability but sacrifices the responsiveness and the bandwidth. Using higher viscosity B_x may be enough to obtain acceptable response with relatively short deadtime (e.g., $T_d = 0.3$ s), but it may not with longer deadtime (e.g., $T_d = 0.6$ s).

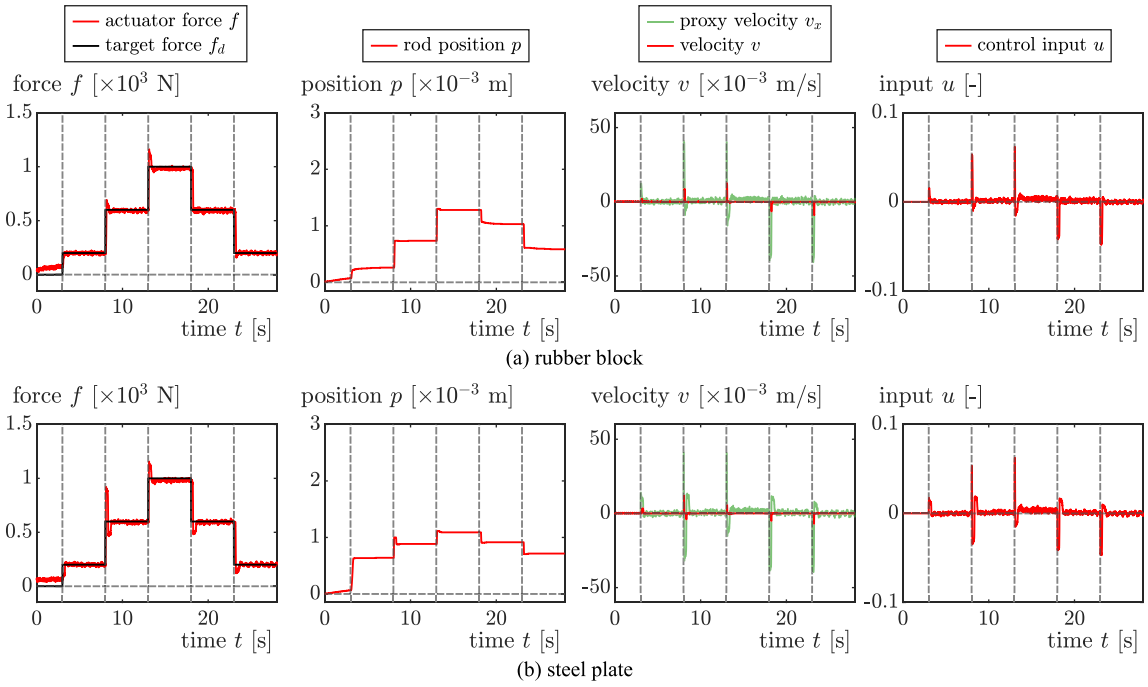

Fig. 9. Results of experiment I in contact with (a) a rubber block and (b) a steel plate with the controller (13).

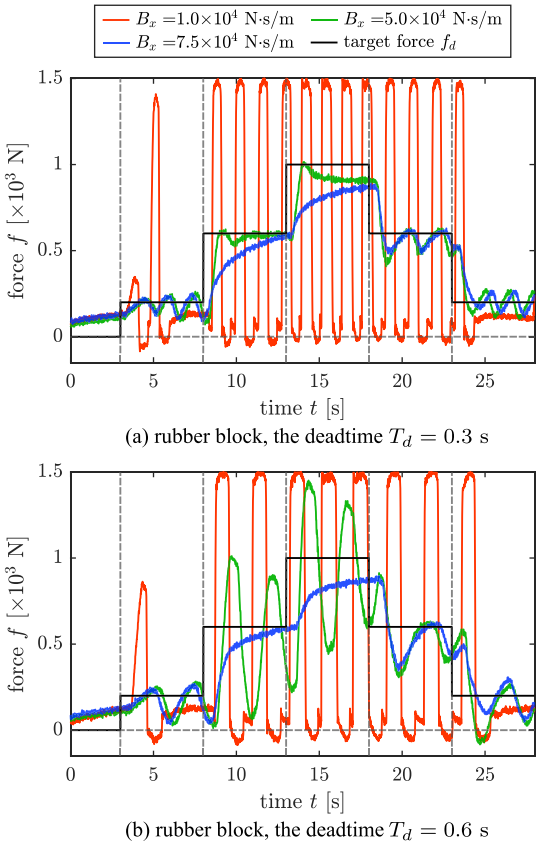

Fig. 10. Results of experiment II with three different values of the proxy viscosity B_x in the controller (13): (a) the deadtime $T_d = 0.3$ s and (b) the deadtime $T_d = 0.6$ s. (For interpretation of the references to color in this figure legend, the reader is referred to the web version of this article.)

5.5. Experiment III : Force controller with stabilizer

Another set of experiments was performed to validate the stabilizer-embedded controller (36), which is to achieve stability without heightening the viscosity B_x. In these experiments, a software deadtime was inserted, and the viscosity was set as $B_x = 1.0 \times 10^4$ N s/m, which was the lowest among those used in Experiment II. The rubber block was used as the environment, and the target force f_d was given as a step-like signal.

Fig. 11 shows the results. the software deadtime T_d was set as 0.3 s in the experiments of Fig. 11(a) and (b). Fig. 11(a) shows the result with the proposed controller (13) only, i.e., without the stabilizer. In the case without the stabilizer, the force f and the position p oscillated and the actuator rod repeatedly bounced on the environment and could not establish stable contact. Fig. 11(b) shows the result with the stabilizer-embedded controller (36), of which the parameter $\hat{T}_d$, the estimated deadtime, was set to 0.3 s (= T_d). Fig. 11(b) shows that the force f was significantly stabilized by the stabilizer. From the graphs of the velocity v in Fig. 11, it can be observed that the stabilizer effectively suppresses the proxy velocity v_x from its original value plotted in green to its suppressed value plotted in blue.

Fig. 11(c) shows the result with the deadtime $T_d = 0.6$ s. In this experiment, the actuator force f smoothly followed the target force f_d, exhibiting the effect of the stabilizer, although a longer T_d resulted in lower accuracy. From the comparison between the results in Fig. 11(b) and (c), the force error in Fig. 11(b) with $T_d = 0.6$ s was larger than that in Fig. 11 with $T_d = 0.3$ s. It can be attributed to the inaccuracy of V^*_{RE}, which is the estimated energy after the deadtime, and the error of V^*_{RE} can be seen from the graphs of the energy in Fig. 11. The force error might be able to be reduced by using more accurate values of the stiffness K_r and the mass M, but these experimental results suggest that such roughly estimated values of stiffness and mass parameters are enough to realize fairly accurate force control.

Fig. 11(d) shows the result with a longer deadtime $T_d = 1.2$ s. Although the force f did not diverge, the magnitude of oscillations became larger and the frequency became lower than the results shown in Fig. 11(b)(c), of which the deadtime is shorter. It should be noted that, even under a larger deadtime T_d, the velocity v does not become

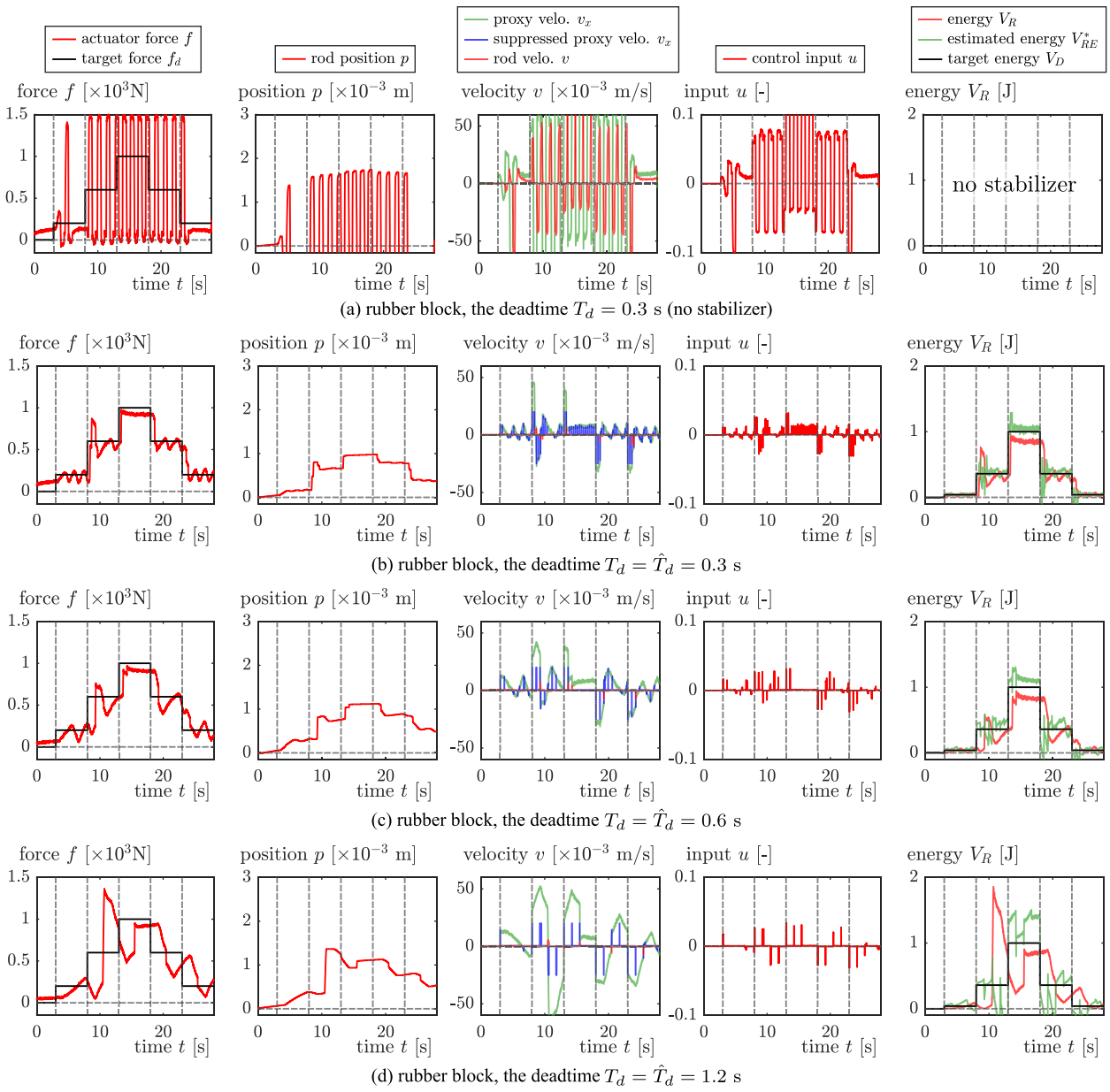

Fig. 11. Results of experiment III in contact with a rubber block with a software deadtime: (a) the controller (11) with the software deadtime $T_d = 0.3$ s, and (b)(c)(d) the stabilizer-embedded controller (36) with the software deadtime $T_d = \hat{T}_d = 0.3$ s, $T_d = \hat{T}_d = 0.6$ s, and $T_d = \hat{T}_d = 1.2$ s, respectively. The bounds of the proxy velocity were set as $[v_N, v_P] = [-2.5 \times 10^{-2}\ \text{m/s}, 5.0 \times 10^{-4}\ \text{m/s}]$ and $[v_n, v_P] = [-1.0 \times 10^{-4}\ \text{m/s}, 2.0 \times 10^{-2}\ \text{m/s}]$. (For interpretation of the references to color in this figure legend, the reader is referred to the web version of this article.)

larger because of the bound $[v_N, v_P]$ imposed by the stabilizer.

By comparing the graphs of the force f in Fig. 11 with those in Fig. 10, one can observe that the effect of the stabilizer is quite different from that of the increased proxy viscosity B_x. Although both the stabilizer and the proxy viscosity B_x work to suppress the proxy velocity v_x, the stabilizer realizes quicker responses while maintaining the stability.

Although not included here for the conciseness of the paper, similar experiments were performed with the steel plate. Step responses were stable with the software deadtime of $T_d = 0.6$ s with the stabilizer, though larger oscillations and overshoots were observed compared to those with the rubber block.

5.6. Experiment IV : Effects of error in estimated deadtime

In practical uses, it is not always possible to obtain an accurate value for the true deadtime T_d. To check the influence of errors in the estimated deadtime $\hat{T}_d$ in the stabilizer-embedded controller (36), several experiments were conducted with seven different values of the estimated deadtime $\hat{T}_d$ for the setup with the true deadtime $T_d = 0.3$ s or 0.6 s. The rubber block was used as the environment.

Fig. 12(a) shows the experimental results with the deadtime $T_d = 0.3$ s and the estimated deadtime $\hat{T}_d \in \{0\text{ s}, 0.1\text{ s}, 0.2\text{ s}, 0.3\text{ s}, 0.4\text{ s}, 0.5\text{ s}, 0.6\text{ s}\}$. In conclusion, the smaller the error between T_d and $\hat{T}_d$, the better the results, with smaller oscillations or smaller steady-state errors. More specifically, the results are prone to oscillations with underestimated deadtime ($\hat{T}_d < T_d$), and to steady-state error with

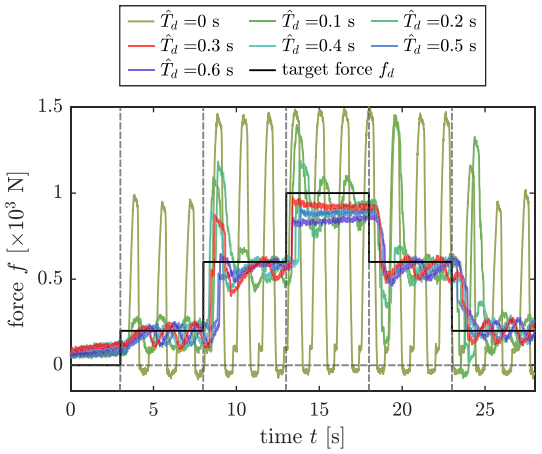

(a) rubber block, the deadtime $T_d = 0.3$ s

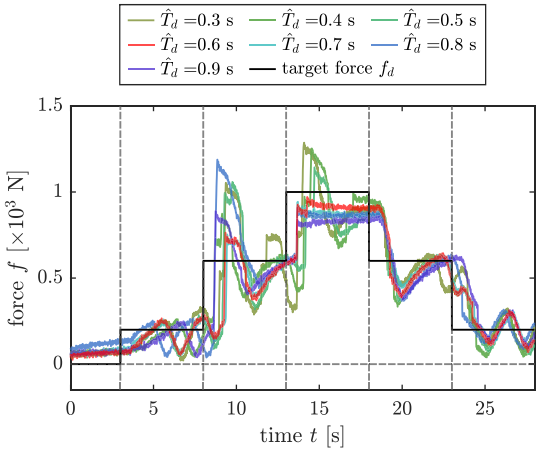

(b) rubber block, the deadtime $T_d = 0.6$ s

Fig. 12. Results of experiment IV with seven different values of the estimated deadtime $\hat{T}_d$: (a) the true deadtime $T_d = 0.3$ s and (b) the true deadtime $T_d = 0.6$ s. The red lines show the results with $\hat{T}_d = T$. (For interpretation of the references to color in this figure legend, the reader is referred to the web version of this article.)

overestimated deadtime ($\hat{T}_d > T_d$), which can be seen in $t \in [13\text{ s}, 18\text{ s}]$. Fig. 12(b) shows the experimental results with the deadtime $T_d = 0.6$ s and the estimated deadtime $\hat{T}_d \in \{0.3\text{ s}, 0.4\text{ s}, 0.5\text{ s}, 0.6\text{ s}, 0.7\text{ s}, 0.8\text{ s}, 0.9\text{ s}\}$. It also shows that the smaller the error between T_d and $\hat{T}_d$, the better the results, and the smaller values of $\hat{T}_d$ tend to result in large oscillations.

These results in Fig. 12 suggest that, when the plant deadtime T_d is not accurately available, it is safe to set the estimated deadtime $\hat{T}_d$ as a large value within a practical range. After that, it should be gradually reduced through some trial-and-error, until achieving acceptable responses.

5.7. Experiment V : Tracking to chirp command

As mentioned in Remark 4, the stability analysis in Theorem 2 does not cover the case of force tracking control, where $\dot{f}_d \not\equiv 0$. To empirically investigate the applicability of the controller to tracking control, another set of experiments was performed with a chirp target force command f_d, of which the frequency was increased from 0.125 Hz to 0.4 Hz. The rubber block was used as the environment.

The results of the controller (11), without deadtime, are shown in Fig. 13(a). It is shown that the force f with the controller (11) closely

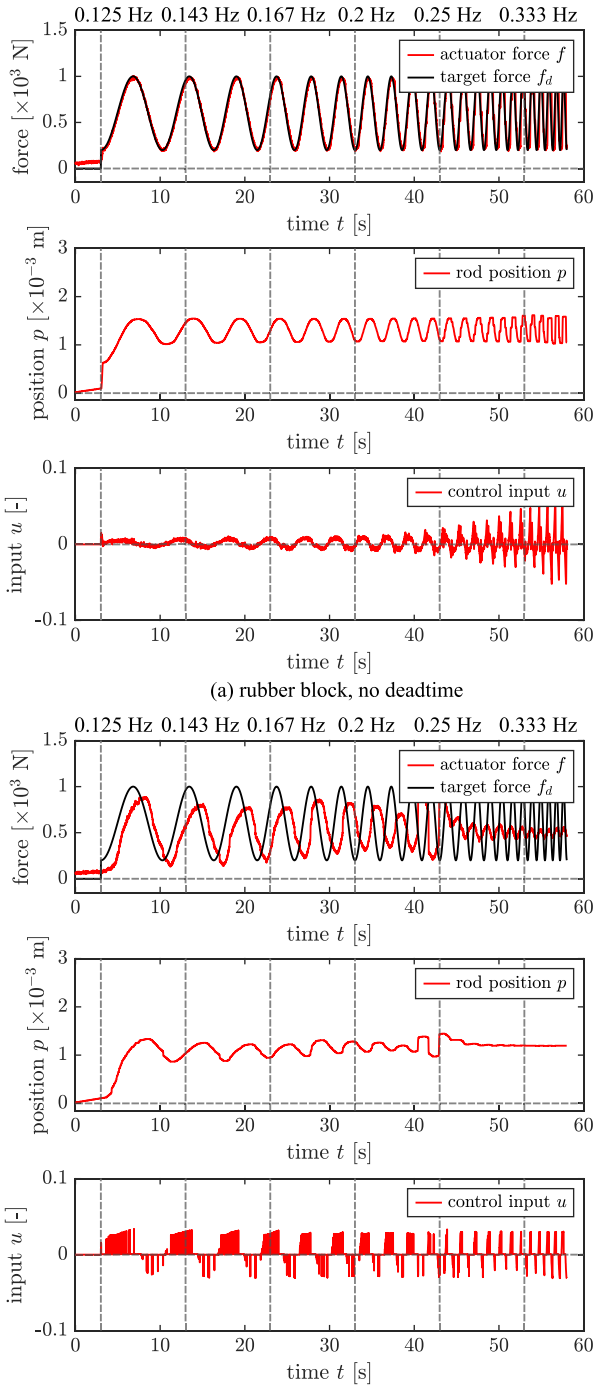

(a) rubber block, no deadtime

(b) rubber block, the deadtime $T_d = \hat{T}_d = 0.6$ s

Fig. 13. Results of experiment V with a chirp target command f_d, of which the period was increased by 0.1 from 8 s to 2.5 s: (a) the controller (13) without a software deadtime and (b) the stabilizer-embedded controller (36) with a software deadtime $T_d = \hat{T}_d = 0.6$ s.

tracks the target force f_d across the entire frequency range.

The results of the stabilizer-embedded controller (36) under the software deadtime $T_d = 0.6$ s are shown in Fig. 13(b). It is shown that the force f tracks the target force f_d with a lag, and its magnitude becomes smaller at frequencies higher than 0.25 Hz, indicating a limited bandwidth of the stabilizer-embedded controller (36) under a large

deadtime $T_d = 0.6$ s. It should however be noted that the stability is maintained even under this deadtime, which would cause instability without the stabilizer.

These results suggest that the controller (11) is applicable as a force tracking controller if the plant deadtime is small enough, and the stabilizer-embedded controller (36) is applicable to the plant under deadtime at least as a force set-point controller, and also as a band-limited force tracking controller.

6. Conclusion

This paper has proposed a force controller for hydraulic actuators. The structure of the proposed controller is similar to the admittance controller and is described only by two equations; one is the virtual admittance model and the other is an actuator model, which is used to command the opening ratio of the main control valve of the actuator. To address the actuator deadtime, an energy-based stabilizer has been proposed and embedded within the force controller. The proposed controller and stabilizer have been validated through experiments using a hydraulic setup with the deadtime of 0.3 s or 0.6 s. The experimental results show that the proposed method realizes stable contact-force control against a rubber block and a steel plate, with a certain level of robustness.

CRediT authorship contribution statement

Yuki Yamamoto: Writing – review & editing, Writing – original draft, Visualization, Validation, Software, Methodology, Investigation, Formal analysis, Data curation, Conceptualization. **Ryo Kikuuwe:** Writing – review & editing, Supervision, Formal analysis.

Declaration of competing interest

The authors declare that they have no known competing financial interests or personal relationships that could have appeared to influence the work reported in this paper.

Acknowledgments

This work is supported by Kobelco Construction Machinery Co., Ltd. and also by JSPS KAKENHI grant number JP 23KJ1622.

References

Acary, V., & Brogliato, B. (2008). *Lecture notes in applied and computational mechanics: vol. 35, Numerical methods for nonsmooth dynamical systems: applications in mechanics and electronics*. Springer.

Ahn, K. K., Chau, N. H. T., & Truong, D. Q. (2007). Robust force control of a hybrid actuator using quantitative feedback theory. *Journal of Mechanical Science and Technology*, *21*, 2048–2058. http://dx.doi.org/10.1007/bf03177463.

Ahn, K. K., & Dinh, Q. T. (2009). Self-tuning of quantitative feedback theory for force control of an electro-hydraulic test machine. *Control Engineering Practice*, *17*(11), 1291–1306. http://dx.doi.org/10.1016/j.conengprac.2009.06.004.

Akers, A., Gassman, M., & Smith, R. (2006). *Hydraulic power system analysis* (2nd ed.). CRC Press, http://dx.doi.org/10.1201/9781420014587.

Alleyne, A., & Liu, R. (1999). On the limitations of force tracking control for hydraulic servosystems. *Transactions of ASME: Journal of Dynamic Systems, Measurement, and Control*, *121*(2), 184–190. http://dx.doi.org/10.1115/1.2802453.

Alleyne, A., & Liu, R. (2000). A simplified approach to force control for electro-hydraulic systems. *Control Engineering Practice*, *8*(12), 1347–1356. http://dx.doi.org/10.1016/s0967-0661(00)00081-2.

Boaventura, T., Buchli, J., Semini, C., & Caldwell, D. G. (2015). Model-based hydraulic impedance control for dynamic robots. *IEEE Transactions on Robotics*, *31*(6), 1324–1336. http://dx.doi.org/10.1109/tro.2015.2482061.

Borutzky, W., Barnard, B., & Thoma, J. U. (2002). An orifice flow model for laminar and turbulent conditions. *Simulation Modelling Practice and Theory*, *10*(3–4), 141–152. http://dx.doi.org/10.1016/s1569-190x(02)00092-8.

Chae, Y., Rabiee, R., Dursun, A., & Kim, C.-Y. (2017). Real-time force control for servo-hydraulic actuator systems using adaptive time series compensator and compliance springs. *Earthquake Engineering & Structural Dynamics*, *47*(4), 854–871. http://dx.doi.org/10.1002/eqe.2994.

Chen, S., Chen, Z., & Yao, B. (2018). Precision cascade force control of multi-DOF hydraulic leg exoskeleton. *IEEE Access*, *6*, 8574–8583. http://dx.doi.org/10.1109/access.2018.2801351.

Chen, S., Chen, Z., Yao, B., Zhu, X., Zhu, S., Wang, Q., et al. (2017). Adaptive robust cascade force control of 1-DOF hydraulic exoskeleton for human performance augmentation. *IEEE/ASME Transactions on Mechatronics*, *22*(2), 589–600. http://dx.doi.org/10.1109/tmech.2016.2614987.

Cheng, L., Zhu, Z.-C., Shen, G., Wang, S., Li, X., & Tang, Y. (2020). Real-time force tracking control of an electro-hydraulic system using a novel robust adaptive sliding mode controller. *IEEE Access*, *8*, 13315–13328. http://dx.doi.org/10.1109/access.2019.2895595.

Cristofori, D., & Vacca, A. (2015). Modeling hydraulic actuator mechanical dynamics from pressure measured at control valve ports. *Proceedings of the Institution of Mechanical Engineers, Part I: Journal of Systems and Control Engineering*, *229*(6), 541–558. http://dx.doi.org/10.1177/0959651814568366.

Dakova, S., Sawodny, O., & Böhm, M. (2024). Force tracking control for hydraulically actuated adaptive high-rise buildings. *Control Engineering Practice*, *146*, Article 105899. http://dx.doi.org/10.1016/j.conengprac.2024.105899.

Dyke, S. J., Spencer, B. F., Jr., Quast, P., & Sain, M. K. (1995). Role of control–structure interaction in protective system design. *Journal of Engineering Mechanics*, *121*(2), 322–338. http://dx.doi.org/10.1061/(asce)0733-9399(1995)121:2(322).

Essa, M. E.-S. M., Aboelela, M. A., Moustafa Hassan, M. A., & Abdrabbo, S. M. (2018). Model predictive force control of hardware implementation for electro-hydraulic servo system. *Transactions of the Institute of Measurement and Control*, *41*(5), 1435–1446. http://dx.doi.org/10.1177/0142331218784118.

Essa, M. E.-S. M., Aboelela, M. A., Moustafa Hassan, M. A., & Abdrabbo, S. M. (2019). Design of model predictive force control for hydraulic servo system based on cuckoo search and genetic algorithms. *Proceedings of the Institution of Mechanical Engineers, Part I: Journal of Systems and Control Engineering*, *234*(6), 701–714. http://dx.doi.org/10.1177/0959651819884746.

Ferraguti, F., Landi, C. T., Sabattini, L., Bonfè, M., Fantuzzi, C., & Secchi, C. (2019). A variable admittance control strategy for stable physical human–robot interaction. *The International Journal of Robotics Research*, *38*(6), 747–765. http://dx.doi.org/10.1177/0278364919840415.

Haninger, K., Radke, M., Vick, A., & Kruger, J. (2022). Towards high-payload admittance control for manual guidance with environmental contact. *IEEE Robotics and Automation Letters*, *7*(2), 4275–4282. http://dx.doi.org/10.1109/lra.2022.3150051.

He, S. (2009). Neural predictive force control for a hydraulic actuator: Simulation and experiment. *Applied Artificial Intelligence*, *23*(2), 151–167. http://dx.doi.org/10.1080/08839510802631752.

Heinrichs, B., Sepehri, N., & Thornton-Trump, A. B. (1997). Position-based impedance control of an industrial hydraulic manipulator. *IEEE Control Systems*, *17*(1), 46–52. http://dx.doi.org/10.1109/37.569715.

Hiriart-Urruty, J.-B., & Lemaréchal, C. (2001). *Fundamentals of convex analysis*. Springer.

Hyon, S.-H., Suewaka, D., Torii, Y., & Oku, N. (2017). Design and experimental evaluation of a fast torque-controlled hydraulic humanoid robot. *IEEE/ASME Transactions on Mechatronics*, *22*(2), 623–634. http://dx.doi.org/10.1109/tmech.2016.2628870.

Jerouane, M., Sepehri, N., & Lamnabhi-Lagarrigue, F. (2004). Dynamic analysis of variable structure force control of hydraulic actuators via the reaching law approach. *International Journal of Control*, *77*(14), 1260–1268. http://dx.doi.org/10.1080/00207170412331305579.

Khalil, H. K. (2002). *Nonlinear systems* (3rd ed.). Prentice Hall.

Kikuuwe, R. (2019). Torque-bounded admittance control realized by a set-valued algebraic feedback. *IEEE Transactions on Robotics*, *35*(5), 1136–1149. http://dx.doi.org/10.1109/tro.2019.2920069.

Kikuuwe, R., Okada, T., Yoshihara, H., Doi, T., Nanjo, T., & Yamashita, K. (2021). A nonsmooth quasi-static modeling approach for hydraulic actuators. *Transactions of ASME: Journal of Dynamic Systems, Measurement, and Control*, *143*(12), 2196–2206. http://dx.doi.org/10.1115/1.4051894.

Kikuuwe, R., Yamamoto, Y., & Brogliato, B. (2022). Implicit implementation of nonsmooth controllers to nonsmooth actuators. *IEEE Transactions on Automatic Control*, *67*(9), 4645–4657. http://dx.doi.org/10.1109/tac.2022.3163124.

Kim, S.-W., Cho, B., Shin, S., Oh, J.-H., Hwangbo, J., & Park, H.-W. (2021). Force control of a hydraulic actuator with a neural network inverse model. *IEEE Robotics and Automation Letters*, *6*(2), 2814–2821. http://dx.doi.org/10.1109/lra.2021.3062353.

Lichtarowicz, A., Duggins, R. K., & Markland, E. (1965). Discharge coefficients for incompressible non-cavitating flow through long orifices. *Journal of Mechanical Engineering Science*, *7*(2), 210–219. http://dx.doi.org/10.1243/jmes_jour_1965_007_029_02.

Liem, D. T., Truong, D. Q., Park, H. G., & Ahn, K. K. (2016). A feedforward neural network fuzzy grey predictor-based controller for force control of an electro-hydraulic actuator. *International Journal of Precision Engineering and Manufacturing*, *17*(3), 309–321. http://dx.doi.org/10.1007/s12541-016-0039-3.

Liu, C., He, Y., Chen, X., & Cao, H. (2022). Adaptive enhanced admittance force-tracking controller design for highly dynamic interactive tasks. *Industrial Robot*, *49*(5), 903–912. http://dx.doi.org/10.1108/ir-10-2021-0222.

Niksefat, N., & Sepehri, N. (2001). Designing robust force control of hydraulic actuators despite system and environmental uncertainties. *IEEE Control Systems*, *21*(2), 66–77. http://dx.doi.org/10.1109/37.918266.

Ruderman, M. (2017). Full- and reduced-order model of hydraulic cylinder for motion control. In *Proceedings of 43rd annual conference of the IEEE industrial electronics society* (pp. 7275–7280). http://dx.doi.org/10.1109/iecon.2017.8217274.

Ruderman, M., Fridman, L., & Pasolli, P. (2019). Virtual sensing of load forces in hydraulic actuators using second- and higher-order sliding modes. *Control Engineering Practice*, *92*, Article 104151. http://dx.doi.org/10.1016/j.conengprac.2019.104151.

Sivaselvan, M. V., Reinhorn, A. M., Shao, X., & Weinreber, S. (2008). Dynamic force control with hydraulic actuators using added compliance and displacement compensation. *Earthquake Engineering & Structural Dynamics*, *37*(15), 1785–1800. http://dx.doi.org/10.1002/eqe.837.

Smirnov, G. V. (2002). *Introduction to the theory of differential inclusions*. Providence, Rhode Islands, USA: American Mathematical Society.

Truong, D. Q., & Ahn, K. K. (2009). Force control for hydraulic load simulator using self-tuning grey predictor – fuzzy PID. *Mechatronics*, *19*(2), 233–246. http://dx.doi.org/10.1016/j.mechatronics.2008.07.007.

Yamamoto, Y., Qiu, J., Doi, T., Nanjo, T., Yamashita, K., & Kikuuwe, R. (2024). A position controller for hydraulic excavators with deadtime and regenerative pipelines. *IEEE Transactions on Automation Science and Engineering*, 1–17. http://dx.doi.org/10.1109/tase.2024.3354952.

Yamamoto, Y., Qiu, J., Munemasa, Y., Doi, T., Nanjo, T., Yamashita, K., et al. (2021). A sliding-mode set-point position controller for hydraulic excavators. *IEEE Access*, *9*, 153735–153749. http://dx.doi.org/10.1109/access.2021.3128215.

Yang, G., & Yao, J. (2022). Multilayer neuroadaptive force control of electro-hydraulic load simulators with uncertainty rejection. *Applied Soft Computing*, *130*, Article 109672. http://dx.doi.org/10.1016/j.asoc.2022.109672.

Yao, J., Jiao, Z., & Yao, B. (2014). Nonlinear adaptive robust backstepping force control of hydraulic load simulator: Theory and experiments. *Journal of Mechanical Science and Technology*, *28*(4), 1499–1507. http://dx.doi.org/10.1007/s12206-014-0137-z.

Yao, J., Jiao, Z., Yao, B., Shang, Y., & Dong, W. (2012). Nonlinear adaptive robust force control of hydraulic load simulator. *Chinese Journal of Aeronautics*, *25*(5), 766–775. http://dx.doi.org/10.1016/s1000-9361(11)60443-3.

Yu, B., Liu, R., Zhu, Q., Huang, Z., Jin, Z., & Wang, X. (2019). High-accuracy force control with nonlinear feedforward compensation for a hydraulic drive unit. *IEEE Access*, *7*, 101063–101072. http://dx.doi.org/10.1109/access.2019.2929176.

Yu, B., Zhu, Q., Yao, J., Zhang, J., Huang, Z., Jin, Z., et al. (2020). Design, mathematical modeling and force control for electro-hydraulic servo system with pump-valve compound drive. *IEEE Access*, *8*, 171988–172005. http://dx.doi.org/10.1109/access.2020.3012091.

Yuan, H.-B., Na, H.-C., & Kim, Y.-B. (2018). Robust MPC-PIC force control for an electro-hydraulic servo system with pure compressive elastic load. *Control Engineering Practice*, *79*, 170–184. http://dx.doi.org/10.1016/j.conengprac.2018.07.009.

Zhong, H., Li, X., Gao, L., & Dong, H. (2021). Development of admittance control method with parameter self-optimization for hydraulic series elastic actuator. *International Journal of Control Automation and Systems*, *19*(7), 2357–2372. http://dx.doi.org/10.1007/s12555-020-0465-y.

Zhu, W.-H., & Piedboeuf, J.-C. (2004). Adaptive output force tracking control of hydraulic cylinders with applications to robot manipulators. *Transactions of ASME: Journal of Dynamic Systems, Measurement, and Control*, *127*(2), 206–217. http://dx.doi.org/10.1115/1.1898237.